Quadrupolar couplings and magnetic phase diagrams in tetragonal $TmAu_2$

1999 J. Phys.: Condens. Matter 11 1305

(http://iopscience.iop.org/0953-8984/11/5/016)

J. Phys.: Condens. Matter **11** (1999) 1305–1319. Printed in the UK PII: S0953-8984(99)98096-7

Quadrupolar couplings and magnetic phase diagrams in tetragonal $TmAu_2$

P Morin†, Z Kazei‡ and P Lejay§

† Laboratoire Louis Néel, CNRS, BP 166X, 38042 Grenoble-Cédex, France
‡ Laboratory for Magnetism, Physics Department, Moscow State University, 119899 Moscow, Russia
§ CRTBT, CNRS, BP 166X, 38042 Grenoble Cédex, France

Received 5 October 1998

Abstract. The occurrence of a quadrupolar ordering within the γ orthorhombic symmetry at 7 K in $TmAu_2$ ($MoSi_2$-type tetragonal structure) was recently discovered with properties closely reminiscent of the ones observed in isomorphous $TmAg_2$. Both the magnetoelastic couplings and the quadrupolar pair interactions are here determined by means of third-order magnetic susceptibility and parastriction measurements. The existence of an antiferromagnetic ordering around 3 K in the quadrupolar phase leads to complex magnetic phase diagrams in the (H, T) plane, which have been established along the main crystallographic directions of the tetragonal cell and appear to result from the balance between magnetic and quadrupolar interactions.

1. Introduction

The studies of magnetoelastic properties soared in popularity in the seventies for insulating compounds. Rare-earth (R) orthophosphates and orthovanadates are now considered as archetypes of the cooperative Jahn–Teller effect. Several of them exhibit a spontaneous tetragonal–orthorhombic transition (Gehring and Gehring 1975). Large magnetoelastic couplings are also present in R intermetallics and compete with the magnetic interactions (Morin and Schmitt 1990); structural transitions are observed in the paramagnetic range of, for instance, TmZn and $TmAg_2$ (Morin and Rouchy 1993). This coexistence has made necessary the development of microscopic models considering both types of interaction, quadrupolar and magnetic, in the presence of the crystalline electric field (CEF). They demonstrate the relevance of the mean-field approximation to the description of quadrupolar orderings as well as to the analysis of the balance between quadrupolar and spin couplings. Concerning quadrupolar couplings, the main feature is that in insulators, the magnetoelastic coupling clearly dominates the pair interactions mediated by phonons and induces the Jahn–Teller transition, whereas in intermetallics, the quadrupolar ordering is driven by the pair interactions, its best evidence being the spontaneous symmetry lowering associated with the magnetoelastic coupling.

In rare-earth intermetallics, the existence of quadrupolar interactions has been studied mainly for cubic symmetry with record values for the spontaneous magnetostriction (1.7% for the tetragonal symmetry lowering mode in CeZn (Schmitt *et al* 1978)) and with quadrupolar orderings observed in the paramagnetic state as for instance in cubic TmCd and TmZn. In these standard systems, a close coherency has been found between different determinations of the quadrupolar couplings. This has been facilitated by an exact knowledge of the CEF (Morin and Schmitt 1990). Rarer are similar analyses for lower symmetries such as tetragonal or

0953-8984/99/051305+15$19.50

hexagonal owing to the large number of CEF, magnetoelastic and pair interactions coefficients to be determined. The compound $TmAg_2$ ($MoSi_2$-type structure) was the first tetragonal rare-earth intermetallic extensively studied from a quadrupolar point of view; it undergoes at $T_Q = 5$ K a second-order transition to a γ orthorhombic state; no magnetic ordering occurs. The study of its magnetic and magnetoelastic properties was based on an extended susceptibility formalism and leads to a fully coherent understanding of the quadrupolar state. Recently, a similar quadrupolar ordering within the γ orthorhombic symmetry was observed at 7 K in the isomorphous compound $TmAu_2$, with very reminiscent properties (Kosaka *et al* 1998). However, in this last system, an antiferromagnetic ordering occurs around 3 K, i.e. in the orthorhombic phase. These two tetragonal compounds constitute a set reminiscent of cubic TmZn and TmCd. In TmCd and $TmAg_2$, the magnetic bilinear interactions are not large enough to induce a magnetic moment on the singlet ground state and the magnetic system remains undercritical in the ferroquadrupolar phase. In contrast, TmZn and $TmAu_2$ order ferro- and antiferromagnetically, respectively. However in $TmAu_2$, owing to the usual behaviour of an antiferromagnetic system under an applied magnetic field, complex magnetic properties may be expected in particular when studying the (H, T) magnetic phase diagrams.

We present here an extensive study of the magnetic and quadrupolar properties of $TmAu_2$. We first briefly recall the relevant Hamiltonian (section 2) in order to analyse the magnetic and/or quadrupolar response to an applied magnetic field, i.e. the first-order, third-order magnetic susceptibilities, the parastriction associated with different symmetry lowering modes of the tetragonal cell as well as the magnetization processes along the $\langle 100 \rangle$ axes and any direction of the basal plane (section 3). In section 4, low temperature magnetization processes are studied in order to build the magnetic phase diagrams along the principal crystallographic directions.

2. Formalism

The ($\boldsymbol{q} = \boldsymbol{0}$) magnetic properties of the 4f shell are described for a tetragonal symmetry with the following Hamiltonian (Morin *et al* 1988):

$$\mathcal{H} = \mathcal{H}_{CEF} + \mathcal{H}_Z + \mathcal{H}_B + \mathcal{H}_Q + \mathcal{H}_{ME} + (E_{el} + E_B + E_Q). \tag{1}$$

The CEF term, $\mathcal{H}_{CEF}$, is written using the Stevens operator-equivalent method (Stevens 1952) within a system of x, y, z axes parallel to the [100], [010] and [001] axes of the body-centred lattice cell, respectively:

$$\mathcal{H}_{CEF} = \alpha_J V_2^0 O_2^0 + \beta_J (V_4^0 O_4^0 + V_4^4 O_4^4) + \gamma_J (V_6^0 O_6^0 + V_6^4 O_6^4). \tag{2}$$

O_l^m are the Stevens operators, α_J, β_J, γ_J the Stevens coefficients, V_l^m the CEF parameters; we will use in this paper the parameters proposed by Kosaka *et al* (1998). The 4f magnetic moment is coupled through the Zeeman term to the applied magnetic field, $\boldsymbol{H}$, corrected for demagnetizing effects:

$$\mathcal{H}_Z = -g_J \mu_B \boldsymbol{H} \cdot \boldsymbol{J}. \tag{3}$$

The bilinear interactions of Heisenberg type are taken into account within the mean field approximation (MFA):

$$\mathcal{H}_B = -(g_J \mu_B)^2 \frac{\theta}{C} \langle \boldsymbol{J} \rangle \cdot \boldsymbol{J} \tag{4}$$

with C the Curie constant and θ^* the exchange interaction temperature. Within the MFA, the two-ion quadrupolar term reads as

$$\mathcal{H}_Q = -K^\alpha \langle O_2^0 \rangle O_2^0 - K^\gamma \langle O_2^2 \rangle O_2^2 - K^\delta \langle P_{xy} \rangle P_{xy} - K^\varepsilon [\langle P_{yz} \rangle P_{yz} + \langle P_{zx} \rangle P_{zx}] \tag{5}$$

with

$$O_2^0 = 3J_z^2 - J(J+1)$$
$$O_2^2 = J_x^2 - J_y^2$$
$$P_{ij} = \tfrac{1}{2}(J_iJ_j + J_jJ_i) \qquad (ij = xy, yz, zx).$$

Only magnetoelastic contributions linear in strain and restricted to second-rank terms are considered here; in symmetrized notation:

$$\mathcal{H}_{ME} = -(B^{\alpha 1}\varepsilon^{\alpha 1} + B^{\alpha 2}\varepsilon^{\alpha 2})O_2^0 - B^{\gamma}\varepsilon^{\gamma}O_2^2 - B^{\delta}\varepsilon^{\delta}P_{xy} - B^{\varepsilon}(\varepsilon_1^{\varepsilon}P_{zx} + \varepsilon_2^{\varepsilon}P_{yz}). \tag{6}$$

Among the strains ε^{μ}, $\varepsilon^{\alpha I}$ and $\varepsilon_i^{\varepsilon}$ are usually weak in R systems, in particular for intermetallics (see for instance Morin *et al* 1994) and $\varepsilon^{\gamma} = (1/\sqrt{2})(\varepsilon_{xx} - \varepsilon_{yy})$ and $\varepsilon^{\delta} = \sqrt{2}\varepsilon_{xy}$. The B^{μ} are the magnetoelastic coefficients. The related elastic energy is written as

$$E_{el} = \tfrac{1}{2}C_0^{\alpha 1}(\varepsilon^{\alpha 1})^2 + C_0^{\alpha 12}\varepsilon^{\alpha 1}\varepsilon^{\alpha 2} + \tfrac{1}{2}C_0^{\alpha 2}(\varepsilon^{\alpha 2})^2 + \tfrac{1}{2}C_0^{\gamma}(\varepsilon^{\gamma})^2$$
$$+\tfrac{1}{2}C_0^{\delta}(\varepsilon^{\delta})^2 + \tfrac{1}{2}C_0^{\varepsilon}[(\varepsilon_1^{\varepsilon})^2 + (\varepsilon_2^{\varepsilon})^2]. \tag{7}$$

The C_0^{μ} are the symmetrized background elastic constants in the absence of magnetic interactions (for instance $C_0^{\gamma} = (C_{11} - C_{12})_0$ and $C_0^{\delta} = 2(C_{66})_0$). E_B and E_Q are corrective energies, which result from the MFA treatment. Minimizing the free energy with regard to the strains gives the equilibrium strains as functions of the expectation value of the corresponding quadrupolar operators. Replacing these ε^{μ} makes $\mathcal{H}_{ME}$ (equation (6)) indistinguishable from $\mathcal{H}_Q$ (equation 5):

$$\mathcal{H}_Q + \mathcal{H}_{ME} = -G^{\alpha}\langle O_2^0\rangle O_2^0 - G^{\gamma}\langle O_2^2\rangle O_2^2 - G^{\delta}\langle P_{xy}\rangle P_{xy} - G^{\varepsilon}[\langle P_{zx}\rangle P_{zx} + \langle P_{yz}\rangle P_{yz}] \tag{8}$$

with, for the symmetry-lowering modes, $G^{\mu} = G^{\mu}_{ME} + K^{\mu} = (B^{\mu})^2/C_0^{\mu} + K^{\mu}(\mu = \gamma, \delta, \varepsilon)$.

In the $(\boldsymbol{q} = \boldsymbol{0})$ ordered phases or in the presence of large external stresses the Hamiltonian has to be self-consistently diagonalized with regard to the three magnetic components and to the five quadrupolar ones. In the presence of small external stresses, perturbation theory can be applied very fruitfully to the disordered phase. It is then possible to obtain analytical expressions for the free energy associated with each of the five symmetry lowering modes and then to describe the corresponding couplings. For example the third-order magnetic susceptibility, i.e. the H^3 term in the field expansion of the magnetization, reads as:

$$\chi_M^{(3)} = \frac{1}{(1-(\theta^*/C)\chi_0)^4}\left[\chi_0^{(3)} + \frac{2G^{\alpha}(\chi_{\alpha}^{(2)})^2}{1-G^{\alpha}\chi_{\alpha}} + \frac{2G^{\mu}(\chi_{\mu}^{(2)})^2}{1-G^{\mu}\chi_{\mu}}\right]. \tag{9}$$

Only the α-mode is present for H parallel to the [001] axis. χ_0 is the anisotropic magnetic susceptibility. For each symmetry, three single-ion susceptibilities are introduced, which are known as soon as the CEF is determined: $\chi_0^{(3)}$ describes the H^3 term of the magnetic response in the absence of any interaction. The strain susceptibility, $\chi_{\mu} = \partial\langle O_2^{\mu}\rangle/\partial\varepsilon^{\mu}$, is responsible for the softening of the associated elastic constant,

$$C^{\mu} = C_0^{\mu} - \frac{(B^{\mu})^2\chi_{\mu}}{(1-K^{\mu}\chi_{\mu})}. \tag{10}$$

$\chi_{\mu}^{(2)} = \partial\langle O_2^{\mu}\rangle/\partial H^2$ is the quadrupolar response to a magnetic field and determines the parastriction process:

$$\varepsilon^{\mu} = \frac{B^{\mu}}{C_0^{\mu}}\frac{\chi_{\mu}^{(2)}}{(1-G^{\mu}\chi_{\mu})(1-(\theta^*/C)\chi_0)^2}H^2. \tag{11}$$

Each of the ε^{μ} can be determined from the combinations of $\lambda_{\alpha_1\alpha_2\alpha_3}^{\beta_1\beta_2\beta_3}$, relative changes of length induced by a $(\beta_1\beta_2\beta_3)$ magnetic field and measured in appropriate $(\alpha_1\alpha_2\alpha_3)$ directions.

After the determination of the CEF and of the single ion susceptibilities, the fit of the magnetic susceptibility along the [001] axis and in the basal plane provides us with θ^*. The other experiments give the different pairs of B^μ and K^μ coefficients.

3. Determination of the magnetoelastic couplings

All the measurements presented here have been performed on single crystals cut in an ingot grown by the Czochralski method. They were then annealed at 1000 °C for a week. All the analyses have been realized using the CEF parameters proposed by Kosaka *et al*.

3.1. Magnetic susceptibilities

The isothermal magnetization curves were collected along the [001], [100] and [110] directions. The first- and third-order susceptibility values were then deduced from the zero-field extrapolation and the initial slope of Arrott plots, respectively. Within the experimental accuracy, the first-order magnetic susceptibility is isotropic in the basal plane as expected for the tetragonal symmetry. The CEF anisotropy is observed in favour of the basal plane (figure 1); it is clearly larger than in $TmAg_2$, in particular at high temperature, which agrees with a V_0^2 parameter larger in $TmAu_2$ than in $TmAg_2$. The fit of the data indicates very weak bilinear interactions characterized by $\theta^* = 0 \pm 0.5$ K.

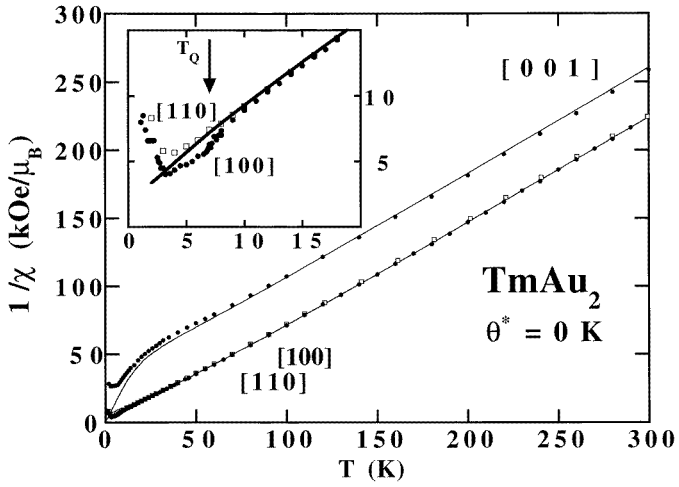

Figure 1. The temperature dependence of the reciprocal first-order susceptibility along the [001] axis and in the basal plane (dots: [100]; open squares: [110]). Full lines are calculated within the tetragonal symmetry for zero magnetic bilinear exchange. T_Q is the γ-quadrupolar transition.

Note that the fit at low temperature along the tetragonal axis is not as perfect as in $TmAg_2$; this could not arise from a misorientation of the field along this axis of difficult magnetization: indeed the measured susceptibility is lower than the calculated one; this seems to indicate a not perfectly optimized set of CEF parameters. The first-order susceptibility along the [001] axis is sensitive to the occurrence of the quadrupolar ordering at T_Q through the reconstruction of the level-scheme and the change in the composition of the wave functions. Along [100], the modification of the susceptibility is due to the same reason with additional effects arising from the partition of the sample into orthorhombic domains (inset of figure 1); fortuitously, the

[110] first-order susceptibility is not significantly sensitive to the quadrupolar ordering. The occurrence of the antiferromagnetic ordering is clearly observed along the three directions.

The $\chi_M^{(3)}$ temperature dependences along the [110] and [001] axes are drawn in figure 2. Along the [001] hard magnetization axis, the third-order magnetic susceptibility is weakly negative; the maximum absolute value is about 1.5×10^{-6} μ_B kOe^{-3} immediately above T_Q. The temperature variation is correctly described with $\theta^* = 0$ K with the raising of a small discrepancy immediately above T_Q. In the orthorhombic phase, it becomes weakly positive. Along the [110] direction, the data are negative; the calculated third-order magnetic susceptibility does not exhibit a significant dependence on G^δ, for G^δ ranging between -100, 100 mK, i.e. absolute values larger than usually observed in rare earth intermetallics. The δ-symmetry is clearly unfavoured by the CEF, the corresponding susceptibilities being weak. In contrast, this third-order magnetic susceptibility quite sizeably depends on the θ^* value and the best fit is obtained with a zero value, as previously observed for the first-order magnetic susceptibility. In this direction also, a small upwards shift is observed for data immediately above T_Q.

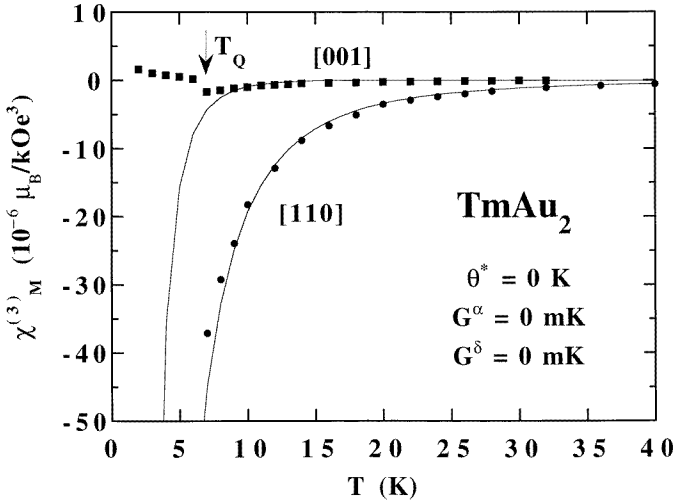

Figure 2. Temperature variation of the third-order magnetic susceptibility along the [110] (dots) and [001] (squares) axes of the body-centred tetragonal cell of $TmAu_2$. Curves are calculated with zero bilinear and quadrupolar contributions.

Along the [100] axis (figure 3), the $\chi_M^{(3)}$ data are positive in the thermal range investigated, in contrast to the values calculated without quadrupolar interactions. Quadrupolar interactions characterized by $G^\gamma = 20$ mK drive the calculated variation to be positive and close to the experimental one. In the vicinity of T_Q, a G^γ value slightly smaller, around 18 mK, would allow one a better fit.

3.2. Parastriction

In order to study the main symmetry lowering modes of the tetragonal cell, magnetostriction data have been collected in a magnetic field applied in the basal plane successively parallel to the [100] and [110] crystallographic directions; strain gauges were glued along the [100], [010] and [110] and [−110] directions, respectively. The isothermal changes of length ($\lambda_\parallel$, $\lambda_\perp$) are then measured parallel and perpendicular to the magnetic field up to 14 T. Within these

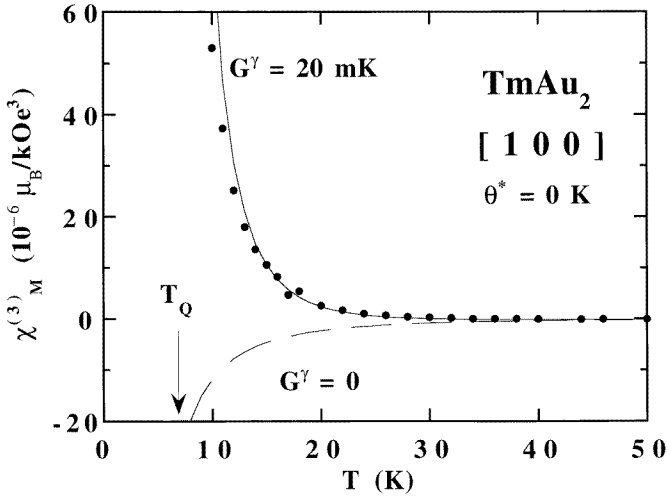

Figure 3. Temperature variation of the third-order magnetic susceptibility along the [100] axis of the body-centred tetragonal cell of $TmAu_2$. Curves are calculated with $\theta^* = 0$ K and γ quadrupolar contributions either null (dashed line) or defined by $G^\delta = 20$ mK (full line).

experimental conditions,

$$\lambda_\parallel = \frac{\varepsilon^{\alpha 1}}{\sqrt{3}} - \frac{1}{\sqrt{6}}\varepsilon^{\alpha 2} + \frac{1}{\sqrt{2}}\varepsilon^{\mu} \text{ and } \lambda_\perp = \frac{\varepsilon^{\alpha 1}}{\sqrt{3}} - \frac{1}{\sqrt{6}} \text{ with } \mu = \gamma \text{or } \delta.$$

At every temperature the quadratic field dependence of the measured change of length has been checked. The fact that $\lambda_\parallel$ and $\lambda_\perp$ are opposite for $\mu = \gamma$ or δ within the experimental accuracy confirms that ε^α contribution is small in comparison to ε^μ. Then the temperature dependence of the initial slope of the difference $\lambda_\parallel = -\lambda_\perp = \sqrt{2}\varepsilon^\mu(H)$ is compared to the predictions from the susceptibility formalism in a linearized form deduced from equation (11).

For the [100] field direction, the difference $\lambda_\parallel - \lambda_\perp = \sqrt{2}\varepsilon^\gamma$ is negative, thus so is B^γ. In figure 4(a), the high temperature slope, $\sqrt{C_0^\gamma/|B^\gamma|} = 59 \pm 1$ MOe, gives without ambiguity the magnetoelastic coefficient value, $B^\gamma = -51.5 \pm 1.5$ K, when using the background elastic constant $C_0^\gamma = 18 \times 10^4$ K defined in Kosaka *et al* (1998) for the fit of the $C^\gamma = C_{11} - C_{12}$ elastic mode.

At low temperature, the same type of discrepancy observed for the third-order magnetic susceptibility in the tetragonal phase is present with an upwards curvature appearing below around 20 K. This phenomenon limits the accuracy of the determination of G^γ, as shown in the inset of figure 4(a); a value of G^γ of 20 ± 2 mK gives however the best agreement above 30 K. This effect also prevents us from observing the 'destraining' effects associated with the partition of the sample into orthorhombic domains below T_Q as done in $TmAg_2$.

This upwards curvature indicates ε^γ to be too small: it is thus not driven by short range order of quadrupolar origin, which would increase the strain. It is more likely due to short range antiferromagnetic order, which reduces the effect of the applied field on the strain. This also agrees with the measured $\chi_M^{(3)}$ absolute values, smaller than the calculated ones at the low temperature of the disordered range, whereas along the [100] direction γ quadrupolar short range order would reinforce the positive $\chi_M^{(3)}$ value. As a general consequence, close to T_Q the G^γ parameter has to slightly move down to a lower value ($G^\gamma = 18$ mK) in order to describe the quadrupolar properties in the present MFA model.

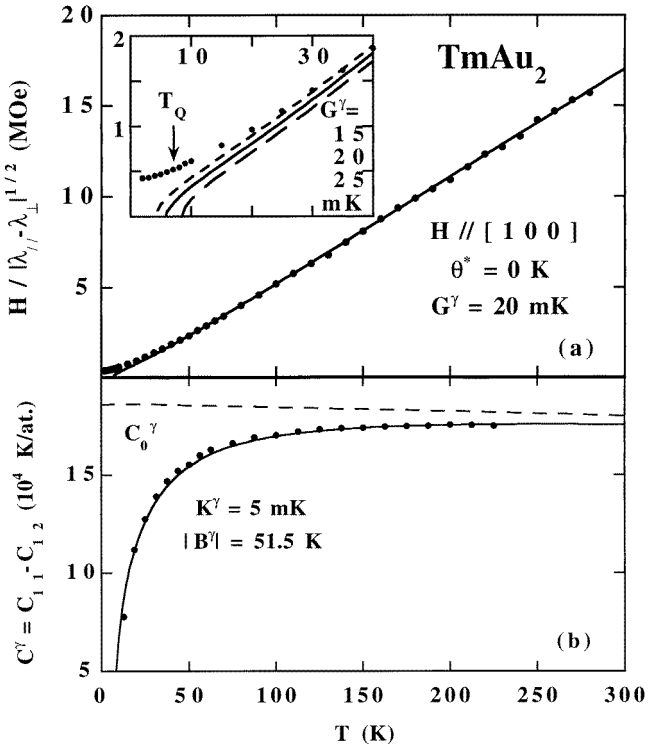

Figure 4. (a) Temperature variation of the parastriction within the γ-symmetry. Curves are calculated with $\theta^* = 0$ K and γ quadrupolar interactions, characterized by the G^γ values indicated. (b) Temperature variation of the $C^\gamma = C_{11} - C_{12}$ elastic mode; data are reported from Kosaka *et al* (1998) and the theoretical variation (full line) is calculated with the quadrupolar parameters deduced from (a) (see text).

The magnetoelastic coefficient here deduced from the slope of $H/\sqrt{\varepsilon^\gamma}$ is larger than in isomorphous $TmAg_2$; this is related to the large background elastic constant determined in Kosaka *et al* (1998) ($C_0^\gamma = 18$ instead of 13.5×10^4 K). The magnetoelastic contribution to $G^\gamma = 20 \pm 2$ mK, $G^\gamma_{ME} = (B^\gamma)^2/C_0^\gamma = 14.5 \pm 0.9$ mK, leads then to a quadrupolar pair coefficient $K^\gamma = 6 \pm 2$ mK. These values are significantly different from the values determined in Kosaka *et al* (1998) ($|B^\gamma| = 33.4$ K and $K^\gamma = 10.6$ mK, $G^\gamma_{ME} = (B^\gamma)^2/C_0^\gamma = 6.2$ mK and $G^\gamma = 16.2$ mK) from the only study of the C^γ ultrasonic mode, the analysis of which is also based on a two-parameter fit. Figure 4(b) shows that the present values of B^γ and K^γ lead to a good fit of C^γ using the same elastic background as in Kosaka *et al* (1998). In conclusion of this study of the γ symmetry-lowering mode, the set of B^γ, K^γ and G^γ leads to coherent descriptions of the T_Q value, the third-order magnetic susceptibility, the parastriction and the C^γ ultrasonic mode (table 1).

At low temperature, the spontaneous orthorhombic strain may be calculated: $\varepsilon^\gamma = B^\gamma/C_0^\gamma\langle O_2^2\rangle \approx -5 \times 10^{-3}$, instead of -4×10^{-3} in $TmAg_2$. The main consequence of the relatively large hardness of the C_0^γ elastic constant observed in Kosaka *et al* (1998), then of the large B^γ magnetoelastic coefficient here deduced is that the ratio of the pair interaction coefficient and the magnetoelastic contribution, $K_\gamma/G^\gamma_{ME} \approx 0.4$, is the smallest observed in rare-earth intermetallics exhibiting a quadrupolar transition. For instance $TmAg_2$, TmZn and

Table 1. Quadrupolar parameters within the γ-orthorhombic symmetry in $TmAu_2$.

	B^μ (K)	K^μ (mK)	G^δ (mK)
$\chi_M^{(3)}$			(18–20)
Parastriction	-51.5 ± 1.5		20 ± 2
$C^\gamma = C_{11} - C_{12}$	-51.5 ± 1.5	5	20
T_Q			22

TmCd are driven to order by the pair interactions ($K_\gamma / G^\gamma_{ME} \approx 1.4$, 4 and 9, respectively), with the more or less efficient help of the magnetoelastic coupling. This latter essentially provides one with the best evidence of the ordering, i.e. the spontaneous symmetry-lowering strain. In contrast, $TmAu_2$ is the first studied intermetallic mainly ordered by the magnetoelastic coupling in a Jahn–Teller process. The large strength of the γ magnetoelastic coupling, observed in $TmAu_2$, has to be confirmed by systematic determinations in the isomorphous RAu_2 compounds.

For the δ-symmetry also, $\lambda_\parallel$ and $\lambda_\perp$ are opposite, but about 20 times smaller than for the γ-symmetry in the same experimental conditions. These small values confirm the weakness of the δ-symmetry-lowering mode, as already proved by the third-order magnetic susceptibility and the absence of any significant softening in the C_{66} temperature variation in figure 4 of Kosaka *et al* (1998). $\lambda_\parallel - \lambda_\perp$ data are positive as is the strain field susceptibility, $\chi_\delta^{(2)}$, thus B^δ is positive. If using as elastic background the $C_0^\delta = 2C_{66}^0 \approx 130 \times 10^4$ K value deduced from Kosaka *et al* (1998) (a value twice that in the RAg_2 series), the slope of the high temperature variation of $\sqrt{C_0^\delta / |B^\delta|}$ would lead to $B^\delta \approx +120$ K, then to $G^\delta_{ME} = (B^\delta)^2 / C_0^\delta = 12$ mK, a value which has no effect on the quadrupolar properties owing to the weakness of the δ quadrupolar susceptibilities. The α quadrupolar mode has been not studied specifically; however for the two modes studied, $\lambda_\parallel + \lambda_\perp = 2(\varepsilon^{\alpha 1}/\sqrt{3} - (1/\sqrt{6})\varepsilon^{\alpha 2})$ is very weak, less than 10^{-2} of the $\lambda_\parallel^{[100]} - \lambda_\perp^{[100]}$ value; the α mode is then quite negligible as observed in $TmAg_2$ and, more generally, in rare earth intermetallics. In conclusion of this section, the γ symmetry-lowering mode is here confirmed to overwhelm the α, δ-symmetry ones.

The quadrupolar parameters here determined, as well as the null θ^* bilinear exchange coefficient, will be kept constant in the following.

3.3. Magnetization in the basal plane

The same quality of the fits is also preserved in the following experiment. The magnetization vector was measured as a function of the orientation of the magnetic field in the basal plane. The sample can rotate round its [001] axis perpendicular to the field. Three pairs of compensated coils measure simultaneously the flux variations parallel and perpendicular to the field during the displacement of the sample parallel to the field. The maximum field is 7.5 T, the accuracy on the magnetic components is about 0.04 μ_B, the positioning angles are determined within ± 0.15 degrees and the temperature is regulated within ± 0.01 K.

The upper parts of figure 5 show the two components, $M_{\parallel H}$ and $M_{\perp H}$, of the paramagnetic moment during the rotation of a constant field in the basal plane, for two temperatures above and below T_Q. The $\pi/2$ periodicity is perfectly respected by the two components. $M_{\parallel H}$ is maximum (minimum) for a field along the $\langle 100 \rangle$ ($\langle 110 \rangle$) axes. As in a torque experiment, $M_{\perp H}$ vanishes as soon as the field points in a high symmetry direction. Its variation is periodic in the experimental conditions, with extrema shifted towards the $\langle 110 \rangle$ axes. The same analysis is valid for the $M_\parallel$ variation; it exhibits an angular point along the $\langle 110 \rangle$ axes, more pronounced in

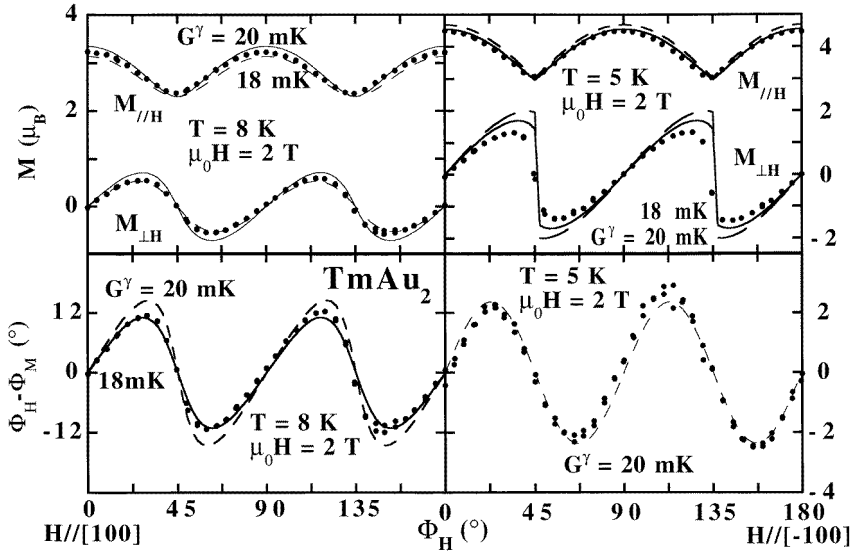

Figure 5. Upper part: components parallel and perpendicular to the field of the paramagnetic moment as functions of the direction of the 2 T field in the basal plane at 8 and 5 K. Lower part: the angle between the field and the paramagnetic moment according to the field direction. Lines are calculated with $\theta^* = 0$ K, $G^\delta = 0$ mK and $G^\gamma = 18$ mK (solid lines) or $G^\gamma = 20$ mK (dashed lines).

the quadrupolar phase. The Φ_H variations of the two components are described by calculations with $G^\delta \in (18, 20$ mK). Note that the effect of the γ symmetry coefficient, G^γ, vanishes for $\Phi_H = 45°$, i.e. $H \parallel \langle 110 \rangle$ in agreement with symmetry considerations. The calculations are presented here for $G^\delta = 0$ mK, but do not significantly depend on G^δ values ranging from -100 to +100 mK. Below T_Q, the partition of the sample in orthorhombic domains is not considered in the calculations. This partition into domains contributes to round off the angular dependence close to the $\langle 110 \rangle$ direction as observed at 5 K. However it can be noted that the experimental variation may be also described using a G^γ coefficient around 16 mK.

From the values of $M_{\parallel H}$ and $M_{\perp H}$, it is possible to calculate the angle, $\phi_H - \phi_M$, between the field and the paramagnetic moment. The variations in the lower parts of figure 5 show that the anisotropies of both the magnetization and the energy are strongly determined by the γ quadrupolar interactions. As soon as $\boldsymbol{H}$ is no longer parallel to the initial [100] axis, the moment moves away from this direction and lies between the field and the closest $\langle 100 \rangle$ axis.

For a magnetic field applied along the [100] direction of the tetragonal phase, the magnetization and its field derivative are closely described at high temperatures as shown in figure 6. Here also, decreasing G^γ parameter values are required when lowering the temperature down to T_Q, which could be a way for our model to compensate the antiferromagnetic short range effect close to T_N.

4. Magnetic phase diagrams

We have then determined the magnetic phase diagrams in the (H, T) plane. Magnetization measurements have been collected down to 1.5 K in the same cryomagnets as previously; additional data have been obtained at lower temperatures using a dilution refrigerator.

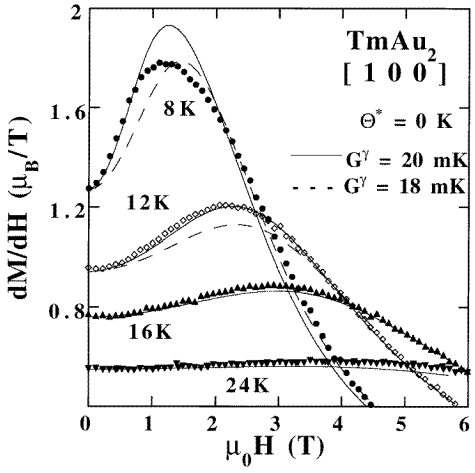

Figure 6. Experimental and calculated field derivative of the magnetization curves along the [100] direction of the tetragonal cell. Lines are calculated with $\theta^* = 0$ K and $G^\gamma = 18$ mK (hatched lines) or $G^\gamma = 20$ mK (solid lines).

Isothermal and isofield measurements have been carried out for the three main directions of the tetragonal symmetry. Isothermal magnetization curves are particularly well suited for locating the transition lines nearly parallel to the horizontal T-axis, while isofield curves are efficient in the case of transition lines more parallel to the vertical H-axis. Except in the low temperature range of the antiferromagnetic range, the transitions are indicated by very subtle anomalies and, to achieve a better accuracy in their determination, the temperature or field derivatives of the magnetization have been used.

4.1. Magnetic phase diagram along the [100] axis

Entering the quadrupolar phase when decreasing the temperature is marked by a change of slope of the isofield magnetization (figure 7). The change in sign of the curvature observed immediately below T_Q between 0.05 and 0.2 T variations is likely due to a more efficient hold of the magnetic field on orthorhombic domains in 0.2 T than in 0.05 T: the increase of the magnetic moment occurs when the majority of the domains have their orthorhombic [100] axis of easy magnetization along the field. As usually, the Néel temperature is marked by a maximum of the isofield magnetization; the temperature dependence of this latter depends on the field value, which reveals the existence of several magnetic phases.

As a function of the field, the isothermal magnetization exhibits two well marked anomalies around 2.5 and 10 kOe for temperatures lower than 2 K; however the high-field transition is broad and the field derivative reveals it to be multiple, triple at 1.6 K (figure 8 upper part). This behaviour exists down to 0.1 K. Broad anomalies, as encountered at 2.0 K, may also correspond to field scans more or less parallel to a vertical transition line in the (H, T) phase diagram. Between about 2.0 K and T_N, the magnetization curves are quite complex as, for instance, the isothermal curves at 2.3 and 2.5 K.

The results of the two types of measurement are reported in figure 9. A good agreement is observed between them and a complex phase diagram is then deduced; the spontaneous phase occurring at T_N, called phase I in the following, is observed to be stable down to 0.1 K. Close to T_N, in fields larger than 4.2 kOe it is replaced by a triangle-shaped phase, phase II. At low

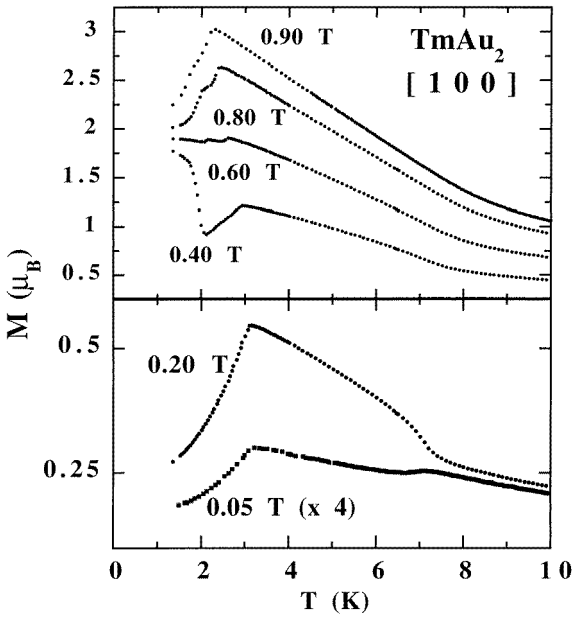

Figure 7. Temperature variation of the isofield magnetic moment measured along the [100] axis for the magnetic fields indicated. Data are collected in decreasing temperature; the values collected in 0.05 T are multiplied by a factor of four.

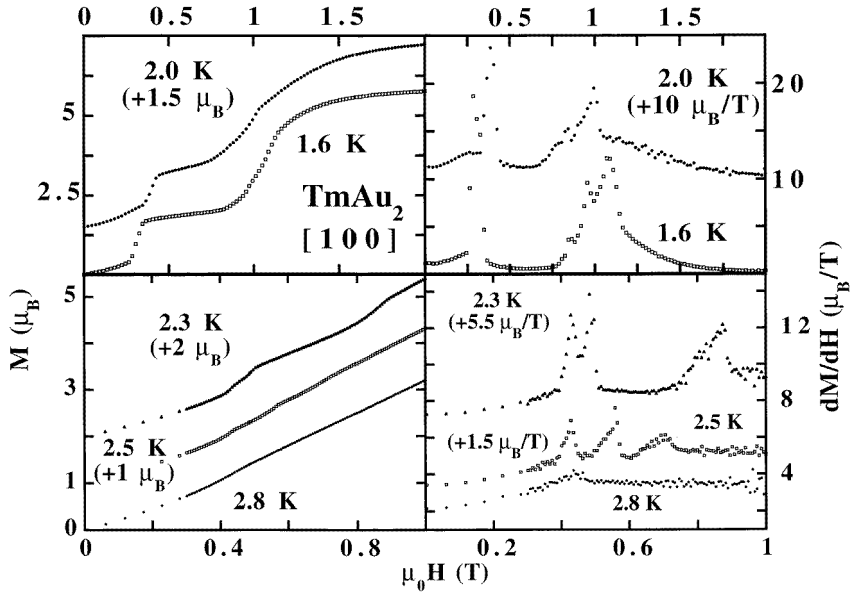

Figure 8. Field dependence of the magnetic moment and its field derivative measured in increasing field parallel to the [100] direction for the temperatures indicated; curves are shifted upwards by the values indicated for each temperature.

temperature and in magnetic fields higher than 2.5 kOe, it vanishes in favour of phase III, characterized by a ferromagnetic component; this latter has a 1.6 μ_B component along the

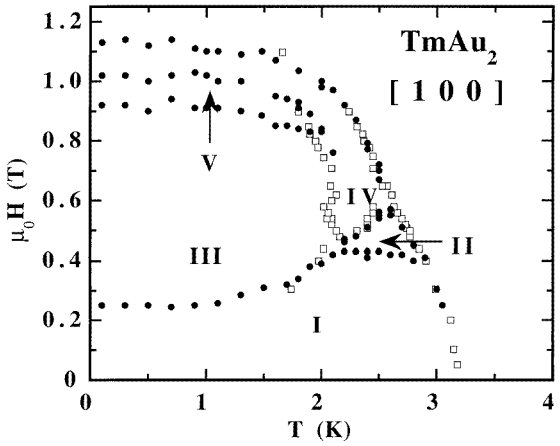

Figure 9. Magnetic phase diagram along the [100] direction (open squares: from temperature variations of the magnetization in constant magnetic fields; black dots: from field variations at constant temperatures).

field direction. Phase III does not spread out up to the paramagnetic phase, being separated from it by phase IV. This latter, very narrow in temperature, then in magnetic field, seems to persist down to 0.1 K. At low temperature, it appears to be separated from phase III by phase V, very narrow in field and not easily defined between them (see the field derivative at 1.6 K in figure 8).

The transition line between antiferromagnetism and polarized paramagnetism looks as usual in an antiferromagnet and the small low-temperature coordinate, 11 kOe, agrees with the weakness of the antiferromagnetic interactions characterized by $T_N = 3.1$ K; its shape is a little bit less round as usually around the border of phase II. At low temperature, when the anisotropy is fully active, the sequence of the different phases may be qualitatively understood as a kind of devil's staircase from the pure antiferromagnetism towards the polarized paramagnetism. The line between phases I and III may result from the different behaviours under field of the magnetic moments system and the quadrupoles one. Spontaneously in an orthorhombic domain, the magnetic moments are frozen along the [100] easy magnetization axis determined by the quadrupoles (the anisotropy between the [100] easy magnetization and [010] hard magnetization axes was observed to be very large in isomorphous $TmAg_2$). In a small external field, they align themselves perpendicular to the applied field as in any collinear antiferromagnet; thus the quadrupolar axis is also perpendicular to the field, which tends to destroy the quadrupolar ordering and this geometry is quite unfavourable to the minimization of the quadrupolar energy, larger than the bilinear one. In large fields, here larger than 2.5 kOe, this situation becomes unstable and the full system rotates to an Ising-like configuration with the external field parallel to the [100] easy magnetization axis, a fraction of the magnetic moments being reversed in order to give rise to the ferromagnetic component. The positive slope of the phase I–III line in the (H, T) plane results then from the complex balance of the magnetic and quadrupolar energies according to the temperature. In order to be confirmed, this qualitative analysis obviously requires, first, a complete determination of the structure associated with each of the different phases by means of neutron diffraction, second, a quantitative analysis by numerical calculations considering the various couplings as done for the complex magnetic properties of cubic NdZn, also ruled by quadrupolar and magnetic interactions (Amara and Morin 1996).

4.2. Magnetic phase diagram along the [001] and [110] axes

Similar procedures were used for magnetic fields parallel to the [001] axis (figure 10 upper part). Only the transitions corresponding to the quadrupolar and antiferromagnetic orderings are observed in the two magnetization behaviours. Isofield variations give clear indications specially in low fields for almost vertical transition lines and isothermal processes do the same for nearly horizontal transition lines. The magnetic phase diagram is then quite simple and easy to understand at least qualitatively: quadrupoles and magnetic moments point perpendicular to the external field, which has to break both arrangements. The [001] polarized paramagnetic state is achieved when the $\langle O_2^2 \rangle$ quadrupolar component vanishes. As long as it persists, it delays the rotation of the magnetic moments towards the field and allows the antiferromagnetism to exist in higher fields than expected from its weak energy and the only CEF anisotropy. This requires magnetic fields as large as 6 T at 0.1 K.

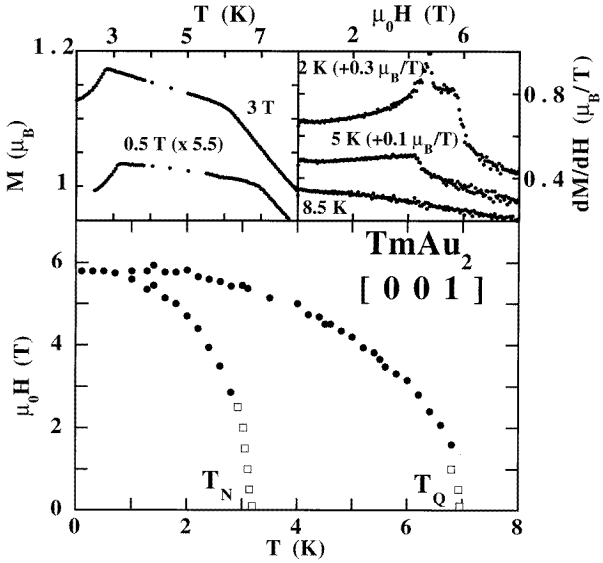

Figure 10. Upper left part: isofield magnetization variations as functions of the temperature; the magnetization values in 0.5 T are multiplied by a factor of 5.5; right part: field derivative of the isothermal magnetization; the 2 and 5 K curves are shifted upwards by 0.3 and 0.1 μ_B T^{-1}, respectively. Lower part: the magnetic and quadrupolar phase diagram deduced for a [001] direction of the applied magnetic field (open squares: from temperature variations of the magnetization in constant magnetic fields; black dots: from field variations at constant temperatures).

Along the [110] axis, no anomaly is observed concerning the quadrupolar ordering; this agrees with symmetry considerations; indeed in the tetragonal phase, a [110] magnetic field can only induce a $\langle P_{xy} \rangle$ quadrupolar component associated with the corresponding δ symmetry. In the orthorhombic phase no clear anomaly may be associated with any modification of the quadrupolar structure. At lower temperatures, in the magnetic range, the magnetization processes are reminiscent of the ones observed along the [100] one (figure 11). The resulting phase diagram consists of the same magnetic phases as along the [100] axis, the critical field values being larger, in a ratio not too far from the cosine of the angle between the two directions. Owing to the profile of the field derivative of the isothermal magnetization around 14 kOe, it appears that phase V does not exist.

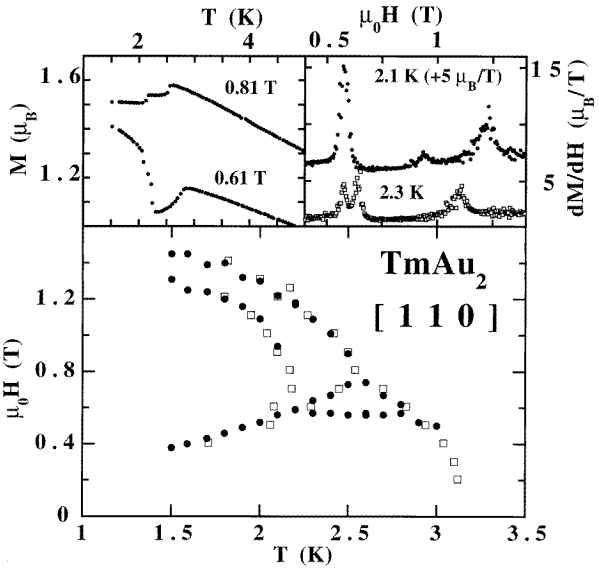

Figure 11. Upper left part: isofield magnetization variations as functions of the temperature; right part: field derivative of the isothermal magnetization; the 2.1 K curve is shifted upwards by 5 μ_B T^{-1}. Lower part: the magnetic phase diagram deduced for a [110] direction of the applied magnetic field (open squares: from temperature variations of the magnetization in constant magnetic fields; black dots: from field variations at constant temperatures).

5. Conclusion

Following the initial study of Kosaka *et al* (1998), we have determined in a first step the strength of the quadrupolar couplings in $TmAu_2$. This compound exhibits properties very reminiscent of the ones observed in isomorphous $TmAg_2$. Their description using the CEF level scheme proposed by Kosaka *et al* is quite satisfactory in the basal plane although reduced discrepancies may exist for properties observed along the tetragonal axis. In particular, the γ quadrupolar coefficients are coherently determined from the analysis of the elastic constant, parastriction and third-order magnetic susceptibility measurements. We may note the existence of some antiferromagnetic short range effects below about 15–20 K. The elastic constants, C^{γ} and C^{δ}, measured by Kosaka *et al* appear harder by a factor of about 4/3 than in $TmAg_2$. Since the γ parastriction is of the same order of magnitude in both compounds, this leads to an absolute value of the magnetoelastic coefficient, B^{γ}, increased by the same ratio in $TmAu_2$. The main consequence is that the balance between the $K\gamma$ pair contribution and the G^{γ}_{ME} magnetoelastic one is modified, this latter term becoming dominant; $TmAu_2$ appears then to be the first rare-earth intermetallic to undergo a quadrupolar transition governed by the magnetoelastic coupling and not by the pair interactions. It is important to check the starting point of this analysis, i.e. the increased hardness of the RAu_2.

The main interest of $TmAu_2$ is the coexistence of quadrupolar interactions with antiferromagnetic ones, large enough to induce an antiferromagnetic ordering in the quadrupolar phase. This coexistence leads to magnetic phase diagrams obviously more complex than in the case of ferromagnetic and ferroquadrupolar orderings belonging to the same tetragonal symmetry as in cubic TmZn. The complexity mainly originates from the conflict between quadrupoles which look for an alignment parallel to the external field and

antiferromagnetic moments which lie along the quadrupolar axis, but prefer to be perpendicular to the field. The remaining problems are to determine the different structures present according to the temperature and field values, which is under way, and to quantitatively explain the magnetic properties using the different couplings here determined.

Acknowledgments

The Laboratoire Louis Néel is a Unité Associée à l'Université Joseph-Fourier, Grenoble. This research is supported, in part, by the Russian Fundamental Science Foundation. One of us, ZK, would like to thank the French Ministère de la Recherche et de la Technologie for its support and the Laboratoire Louis Néel for its hospitality. It is a pleasure to thank C Paulsen and W Wernsdorfer for their kind help for magnetization measurements at low temperatures.

References

Amara M and Morin P 1996 *Physica* B **222** 61–72
Gehring G A and Gehring K A 1975 *Rep. Prog. Phys.* B **38** 1
Kosaka M, Onodera H, Ohoyama K, Ohashi M, Yamaguchi Y, Nakamura S, Goto T and Ikeda S 1998 *Phys. Rev.* B **58** 6339
Morin P and Rouchy J 1993 *Phys. Rev.* B **48** 256
Morin P, Rouchy J and Kazei Z 1994 *Phys. Rev.* B **50** 12 625
Morin P, Rouchy J and Schmitt D 1988 *Phys. Rev.* B **37** 5401
Morin P and Schmitt D 1990 *Ferromagnetic Materials* vol 5, ed K H J Buschow and E P Wohlfarth (Amsterdam: North-Holland) p 1
Schmitt D, Morin P and Pierre J 1978 *J. Phys.: Condens. Matter* **8** 7967
Stevens K W H 1952 *Proc. Phys. Soc.* A **65** 209